

# Using Combinatorial Inkjet Printing for Synthesis and Deposition of Metal Halide Perovskites in Wavelength-Selective Photodetectors

Vincent R. F. Schröder, Felix Hermerschmidt,\* Sabrina Helper, Carolin Rehermann, Giovanni Ligorio, Hampus Näsström, Eva L. Unger, and Emil J. W. List-Kratochvil\*

Metal halide perovskites have received great attention in recent years, predominantly due to the high performance of perovskite solar cells. The versatility of the material, which allows the tunability of the bandgap, has led to its use in light-emitting diodes, photo, and X-ray detectors, among other optoelectronic device applications. Specifically in photodetectors, the tunability of the bandgap allows fabrication of spectrally selective devices. Utilizing a combinatorial inkjet printing approach, multiple perovskite compositions absorbing at specific wavelengths in a single printing step are fabricated. The drop-on-demand capabilities of inkjet printing enable the deposition of inks in a precise ratio to produce specific perovskite compositions in the printed thin film. By controlling the halide ratio in the compositions, a mixed halide gradient ranging from pure  $\text{MAPbI}_3$  via  $\text{MAPbBr}_3$  to  $\text{MAPbCl}_3$  is produced. The tunability in the absorption onset from 410 to 790 nm is demonstrated, covering the whole visible spectrum, with a precision of 8 nm steps for  $\text{MAPb}(\text{Br}_x\text{Cl}_{1-x})_3$  compositions. From this range of mixed halide perovskites, photodetectors which show spectral selectivity corresponding to the measured absorption onset are demonstrated, paving the way for use in a printed visible light spectrometer without the need for a dispersion element.

## 1. Introduction

The exceptional optoelectronic properties combined with the ability to process metal halide perovskite semiconductors from solution have led to comprehensive research results in the field of (opto)electronic applications, including photovoltaic devices,<sup>[1–3]</sup> light-emitting diodes (LEDs),<sup>[4–6]</sup> LASER applications,<sup>[7–9]</sup> as well as X-ray<sup>[10–12]</sup> and photodetectors.<sup>[13–15]</sup> To a large extent, these optoelectronic properties, such as the bandgap, the relative position of the energy levels, and the carrier mobility,<sup>[16]</sup> depend on the ionic composition of the material. Through the multitude of possible perovskite compositions, a great freedom of tunability arises to match the device requirements.<sup>[17–19]</sup> In particular in solar cells, LEDs, and photodetectors, the semiconductor bandgap predefines the specification and function of the according devices, as it governs the absorption and emission wavelengths. Therefore, being able to easily tune the bandgap of a


material through composition variation by combinatorial synthesis is highly advantageous for fabricating a wide range of optoelectronic devices with targeted specifications.

V. R. F. Schröder, E. J. W. List-Kratochvil  
Helmholtz-Zentrum Berlin für Materialien und Energie GmbH  
Hahn-Meitner-Platz 1, 14109 Berlin, Germany  
E-mail: [emil.list-kratochvil@hu-berlin.de](mailto:emil.list-kratochvil@hu-berlin.de)

F. Hermerschmidt, S. Helper, G. Ligorio, E. J. W. List-Kratochvil  
Institut für Physik  
Institut für Chemie  
Humboldt-Universität zu Berlin  
IRIS Adlershof  
Zum Großen Windkanal 2, 12489 Berlin, Germany  
E-mail: [felix.hermerschmidt@hu-berlin.de](mailto:felix.hermerschmidt@hu-berlin.de)

C. Rehermann, H. Näsström, E. L. Unger  
Young Investigator Group Hybrid Materials Formation and Scaling  
Helmholtz-Zentrum Berlin für Materialien und Energie GmbH  
Kekuléstraße 5, 12489 Berlin, Germany

E. L. Unger  
Chemical Physics and NanoLund  
Lund University  
PO Box 124, 22100 Lund, Sweden

 The ORCID identification number(s) for the author(s) of this article can be found under <https://doi.org/10.1002/adem.202101111>.

© 2021 The Authors. Advanced Engineering Materials published by Wiley-VCH GmbH. This is an open access article under the terms of the Creative Commons Attribution License, which permits use, distribution and reproduction in any medium, provided the original work is properly cited.

DOI: 10.1002/adem.202101111

One of the greatest success stories of this tunability is the application of metal halide perovskites in various tandem solar cell technologies. By being able to match the bandgap of halide perovskites to lower-bandgap semiconductors such as silicon and copper indium gallium selenide (CIGS), efficient hybrid tandem solar cells have been demonstrated.<sup>[20,21]</sup> In addition to solar cells, the tunability of the bandgap can also be utilized in perovskite-based LEDs and according display applications to adjust the wavelength of the emitted light over the entire visible spectrum,<sup>[22–24]</sup> while also enabling devices emitting in the near infrared.<sup>[25]</sup> In photodetectors, the bandgap tunability can be taken advantage of to produce a wavelength-specific photoresponse.

Yet, while for solar cells and LEDs, typically only a single material layer with a singular specific bandgap is required to achieve the specified performance; in photodetectors, the accessibility of continuous bandgap tuning over a wide spectral range will pave the way for novel device implementations. This is especially the case when compositional tuning can be combined with the ability to laterally structure the material layer. Metal halide perovskites as a material class provide the necessary versatility in targeting multibandgap devices, due to the aforementioned multitude of available perovskite compositions. Moreover, what makes this approach even more attractive is the fact that a multitude of compositions with different properties can be achieved by a combination of a relatively small set of precursor materials. By, for example, varying the halide ions ( $I^-$ ,  $Br^-$ ,  $Cl^-$ ) and the organic ions (methylammonium  $[MA^+]$  or formamidinium  $[FA^+]$ ), a range of active layers can be targeted using a combinatorial synthesis approach of the metal halide perovskite composition. To fully exploit this concept, it is desirable to not only mix the material precursor composition *ex situ*, but also to be able to accomplish mixing with structured deposition of the active layer *in situ*. Using an inkjet printing process with multiple printheads, it is possible to achieve this.<sup>[26–28]</sup>

Inkjet printing as such has already been successfully used as a deposition method for organic semiconductors,<sup>[29]</sup> inorganic semiconductors,<sup>[30]</sup> and metal inks<sup>[31–33]</sup> for the fabrication of various electronic and optoelectronic devices.<sup>[34–37]</sup> More recently, inkjet printing has also been successfully used to deposit metal halide perovskites and perovskite nanocrystal-based optoelectronic devices such as solar cells,<sup>[38]</sup> LEDs,<sup>[39]</sup> and photodetectors.<sup>[40,41]</sup>

Inkjet printing is an additive, a mask-less, and noncontact deposition method, which has the ability to produce functional devices with a high degree of customization, minimal consumption of active material, and selective and structured patterning due to its drop-on-demand (DoD) character.<sup>[42,43]</sup> Moreover it is also an industrially mature and scalable, digital production technology, with the ability to be implemented in high-throughput and large-area industrial-scale production processes.<sup>[44]</sup>

By now combining (at least) two printheads during printing, the simultaneous deposition of (at least) two inks within one coating process is possible and this combinatorial method has been used previously to screen material compositions<sup>[26–28]</sup> for application in solar cells.<sup>[45,46]</sup> In this way, the mixing of ink droplets during deposition on the substrate serves as a combinatorial synthesis and structuring approach, producing a precise ionic composition of the perovskite precursors. Based on these accomplishments, in this contribution, we will use this approach

for the first time to directly fabricate a series of photodetectors with a spectral response spanning the entire visible spectrum. As we are able to stepwise match the spectral response, this work lays the foundation for integrating perovskite-based photodetectors into a visible light spectrometer without the need for a dispersion element.

## 2. Results and Discussion

During the printing procedure, a defined number of ink droplets is deposited on a substrate. The area wetted by a single droplet is determined by the interplay of surface free energy and the surface tension of the ink. The resolution of the printed image in drops per inch (dpi) is chosen in a way that the deposited droplets spread on the surface and merge on contact to form a closed continuous wet film with a thickness of multiple micrometers.<sup>[47]</sup> Starting with the first ink droplet, evaporation of the solvent is initiated, which has to be taken into account when choosing the printing speed. The drying process can result in inhomogeneous films (coffee ring effect)<sup>[48]</sup> and for metal halide perovskites is connected to the crystallization process. Compared with organic semiconductors, the metal halide perovskite is formed during drying. Therefore, controlling the drying process, and by that the crystallization of the perovskite, is crucial for the material quality and performance of the resulting optoelectronic devices. The drying process can be assisted by annealing, vacuum drying, or gas flow-assisted drying.<sup>[39,49]</sup>

Starting with three different print heads filled with three different MA lead halide perovskite precursor inks ( $MAPbI_3$ ,  $MAPbBr_3$ , and  $MAPbCl_3$ ), a gradient of mixing ratios was inkjet printed by varying the relative halide ion concentration. Using the DoD capabilities of inkjet printing and controlling the ratio of deposited droplets of each ink, precise compositional mixing can be achieved. This is enhanced by choosing fully miscible solvent systems, in our case dimethyl formamide : dimethyl sulfoxide (DMF:DMSO),<sup>[50]</sup> and a print pattern that deposits drops deliberately on top of each other to ensure mixing of the inks.

**Figure 1a** displays a schematic depiction of the combinatorial printing process, where droplets of different precursor inks are mixed with different ratios. Within the first half of the gradient (i.e., a combination of  $MAPbI_3$  with  $MAPbBr_3$ ), we incrementally reduced the number of droplets containing the iodide ( $MAPbI_3$ ) precursor and simultaneously increased the number of droplets containing the bromide ( $MAPbBr_3$ ) precursor. In doing so, it is possible to achieve gradient mixtures between a pure iodide and a pure bromide composition, producing perovskite films with the nominal composition of  $MAPb(I_{1-x}Br_x)_3$ . Within the second half of the gradient (i.e., combination of  $MAPbBr_3$  with  $MAPbCl_3$ ), we decreased the number of droplets containing the bromide ( $MAPbBr_3$ ) precursor and simultaneously increased the number of droplets containing the chloride ( $MAPbCl_3$ ) precursor. In this way perovskite films with the nominal composition of  $MAPb(Br_{1-x}Cl_x)_3$  were synthesized. The droplets mix in the desired ratio on the substrate by controlling the position and pairing of the different inks. All the substrates were thermally treated after deposition. Iodide-containing samples were treated at 100 °C for 10 min, and chloride-containing samples were treated at 80 °C for 10 min.

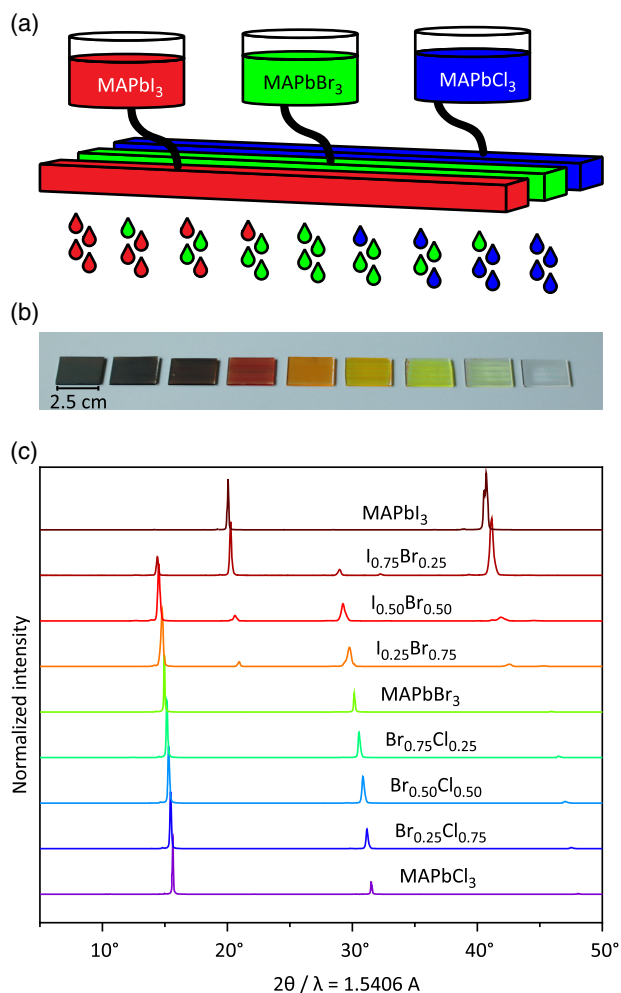


**Figure 1.** a) Combinatorial printing allows precise control of the mixing of perovskite precursor inks during film fabrication. b) This leads to a compositional halide gradient in methylammonium-based metal halide perovskites. c) The resulting distinct perovskite phases are confirmed by the gradual shift of lattice parameters shown in XRD diffraction patterns.

This leads to a gradient of nine thin films deposited on glass substrates, with each composition distinguishable by the naked eye (see Figure 1b). The mixing occurs not only macroscopically but also on the atomic scale, leading to clearly distinguishable crystal phases of the desired composition in accordance with Vegard's law.<sup>[51]</sup> These different phases are distinguishable by X-ray diffraction (XRD) analysis and the results are shown in Figure 1c (and zoom-in image in Figure S1a and S2, Supporting Information).

We observe a gradual shift of the reflection peaks, which corresponds to the decreasing size of the unit cell along the gradient. For MAPbI<sub>3</sub>, the first reflection peak belonging to the (110) plane of the tetragonal perovskite phase sits at 14.13°. Substituting iodide ions by bromide ions decreases the size of the unit cell, resulting in the first reflection peak at 14.95°, belonging to the (100) of the cubic perovskite phase of MAPbBr<sub>3</sub>. Further substitution of bromide by chloride results in a shift of the (100) reflection peak to 15.63° for MAPbCl<sub>3</sub>.<sup>[52–54]</sup> The gradual shift of the

reflection peaks fits directly to the compositional gradient targeted with our combinatorial synthesis approach. We note the strong preferential growth in our perovskite thin film, which results in a strong relative intensity of the reflection peaks of the (100) plane in our samples. Comparing the peak broadness at full width at half maximum (FWHM) of the reflection peaks (See Figure S1c, Supporting Information) reveals a broadening for mixed halide perovskite phases relative to the pure halide compositions. This can be caused by crystal size effects, strain, or by ionic heterogeneities in mixed halide perovskites created during crystallization.<sup>[55]</sup> We further observe no peak splitting in the diffraction patterns of the mixed halide perovskite films that could be attributed to the previously reported miscibility gap.<sup>[56]</sup> To support the results of our XRD measurements, we performed energy-dispersive X-ray spectroscopy (EDX) measurements on the printed thin films. In Figure S3, Supporting Information, the EDX spectra for the printed perovskite compositions are displayed showing the gradual substitution of halide ions. Furthermore, the halide distribution was investigated by elemental mapping, showing equal distribution of halide ions. As seen in scanning electron microscopy (SEM) images, the elemental distribution correlates with the morphology of the printed thin films, on the scale of multiple tens of micrometers. Taking the spreading of printed droplets into account, this finding demonstrates full intermixing of ink droplets during formation of the primary wet film.

Having investigated the crystal structure and confirmed the successful synthesis of the desired perovskite compositions in this comprehensive gradient series, we continued with an investigation of the optical and electronic properties.

We investigated the optical properties of this series of printed samples, specifically their absorption properties using UV/vis spectroscopy. The spectra reported in Figure 2a clearly display a shift in the absorption onset as a function of the halide ratio, which covers the entire visible spectral range from 410 nm (MAPbCl<sub>3</sub>) to 790 nm (MAPbI<sub>3</sub>). The absorption onset shifts in ≈30 nm steps in bromide/chloride mixtures and in ≈60 nm steps in iodide/bromide mixtures. Along this gradient, the exciton binding energy decreases with the perovskite composition, as visible by the disappearance of excitonic features in the absorption spectra of iodide-containing perovskite compositions. Values for the exciton binding energies were determined by fitting the absorption onset to the Elliot equation (see Table S1, Supporting Information) and range from 6.12 meV (MAPbI<sub>3</sub>) to 59.20 meV (MAPbCl<sub>3</sub>). These values are in line with previously reported results.<sup>[57,58]</sup> The increase in exciton binding energies is caused by a decrease in the dynamic dielectric constant from iodide via bromide to chloride-containing perovskites,<sup>[59,60]</sup> which is caused by the decreasing polarizability of the halide ions (according to the Clausius–Mossotti relation).<sup>[61]</sup>

While the absorption onsets shift, the steepness varies substantially. Especially iodide-containing perovskite compositions show a more gradual absorption onset, quantified as broadness of the first derivative (see Figure S4, Supporting Information).<sup>[62]</sup> Correlating with the broadening observed in the XRD reflection peaks, the width in the first derivative of the absorption onset gives another experimental indication of the variation in ionic heterogeneity in the mixed halide perovskite compositions.

Furthermore, the advantages of the combinatorial synthesis approach allow us to access even finer compositional differences

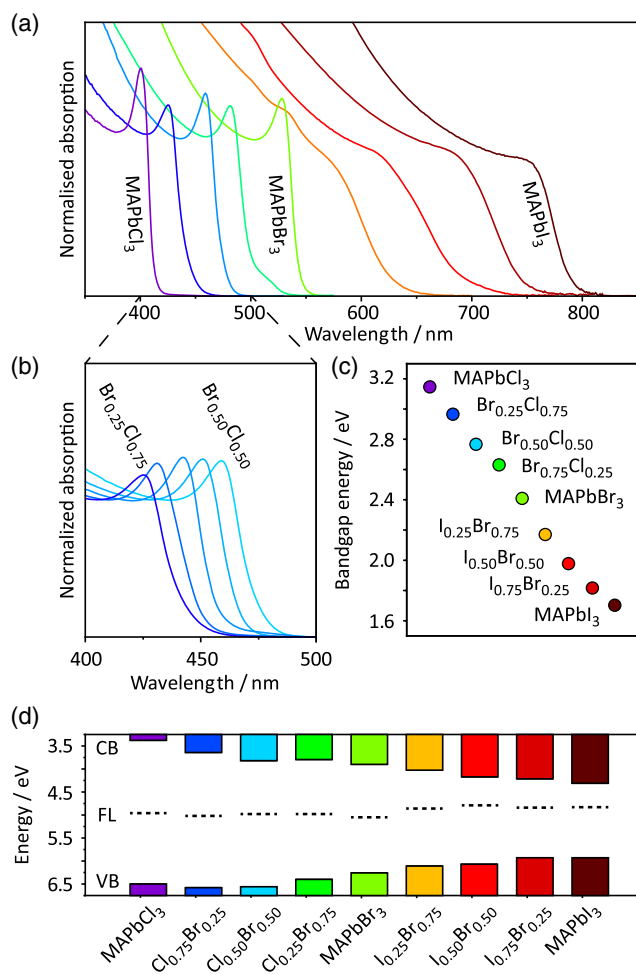


**Figure 2.** a) The printed films show a shifting absorption onset over the full range of the visible spectrum. b) Precise control of the absorption onset can be achieved by fine tuning the composition of deposited perovskite precursors. c) The linear dependence of the extracted bandgaps on the nominal composition of the printed perovskite films confirms the precise control of the combinatorial approach. d) The same linear trend can be observed in the energy-level diagrams consisting of VB, Fermi level (FL), and CB.

by adjusting the combinatorial print pattern. Figure 2b shows the result of the influence on the absorption onset of such an incremental change between the MAPb(Br<sub>0.25</sub>Cl<sub>0.75</sub>)<sub>3</sub> and MAPb(Br<sub>0.5</sub>Cl<sub>0.5</sub>)<sub>3</sub> compositions, allowing a resolution of  $\approx 8$  nm steps between  $\approx 440$  and  $\approx 470$  nm. Fitting the absorption onsets to the Elliot equation yields not only the exciton binding energy but also the bandgap energy. We compiled the extracted bandgap energies in Figure 2c. The extracted bandgaps range from 1.64 eV (MAPbI<sub>3</sub>) to 3.14 eV (MAPbCl<sub>3</sub>) and show a linear dependence, which directly correlate to the linear change of nominal composition of the perovskite layers (the results are reported in Table S1, Supporting Information). After having assessed the optical gap, we conducted the investigation of the energy level by means of ultraviolet photoemission spectroscopy (UPS). This technique provides information of the work function (WF) and hole injection barrier (HIB) extrapolated from secondary

electron cutoff and valence band (VB) onset, respectively. The printed perovskite samples were fabricated employing ITO-coated glass as substrates to ground them during the measurements. The VB is calculated as the ionization potential (IP) given by the sum of the WF and HIB (WF, HIB, and IP are listed in Table S1, Supporting Information). The compositional perovskite series shows an increase in the IP (and with it, the position of the VB) along the gradient of inkjet-printed samples with increasing bromide or chloride content. MAPbI<sub>3</sub>, MAPbBr<sub>3</sub>, and MAPbCl<sub>3</sub> IPs of 5.93 eV, 6.26 eV, and 6.50 eV were determined. These results are in line with previous reported values.<sup>[54,63,64]</sup> The results are confirmed by photoelectron yield spectroscopy (PYS) conducted in air (with the results also summarized in Table S1, Supporting Information). The position of the conduction band (CB) is estimated by subtracting the bandgap from the VB. The constructed energy-level diagrams for the full series of perovskite compositions are shown in Figure 2d. Along the gradient, from MAPbI<sub>3</sub> to MAPbCl<sub>3</sub>, a shift in the position of the VB of  $\approx 0.6$  eV and a shift of the position of the CB of  $\approx 0.9$  eV occur, which is caused by a combination of increasing electronegativity and confinement effects.<sup>[63]</sup>

The shifts in the bandgap and the resulting absorption onset allow the exploitation of this series as photoactive materials in the production of wavelength-selective photodetectors. We therefore fabricated a series of photodetectors (schematically depicted in Figure 3a) by printing this series of nine materials on prepatterned indium tin oxide (ITO) interdigitated electrodes. The photoresponse was measured under constant bias as a function of incident wavelength. By referencing this response to a calibrated silicon solar cell, the external quantum efficiency (EQE) was determined. As depicted in Figure 3b, the spectral response of the photodetectors ranges from 410 nm (MAPbCl<sub>3</sub>) to 790 nm (MAPbI<sub>3</sub>) and matches the absorption spectra discussed earlier. The ionic heterogeneity shown in the XRD reflection peak width and gradual absorption onset has no significant effect on the detection onset of the photodetector devices. To study the behavior of the detection onset during operation, mixed halide perovskite (iodide/bromide) detectors were fabricated and subjected to increasing voltage from 5 to 40 V (see Figure S5a, Supporting Information) and a constant voltage of 30 V over time (see Figure S5b, Supporting Information). In both cases, a shift of the detection onset toward longer wavelengths can be observed, which saturates at a maximum shift of  $\approx 10$  nm. The influence of ionic heterogeneity on the spectral selectivity therefore remains controllable.

In a next step, the photodetectors were each illuminated by different high-powered LEDs ( $\approx 100$ – $300$  mW cm<sup>-2</sup>, peak wavelengths between 375 and 850 nm and FWHM between 10 and 30 nm, as shown in Figure S6, Supporting Information). The photocurrent was measured as a function of the applied bias and we find a linear behavior between  $-5$  and  $5$  V for all devices, as shown in Figure S7, Supporting Information. When a photodetector is illuminated with an LED whose wavelength is longer than the absorption onset of the perovskite material, the resulting photocurrent is in the order of magnitude of the dark current (the black lines). Therefore, for the pure chloride-containing perovskite photodetector, a photoresponse and increase in measured photocurrent are only seen upon illumination with violet and blue light. As we continue along the gradient and shift the



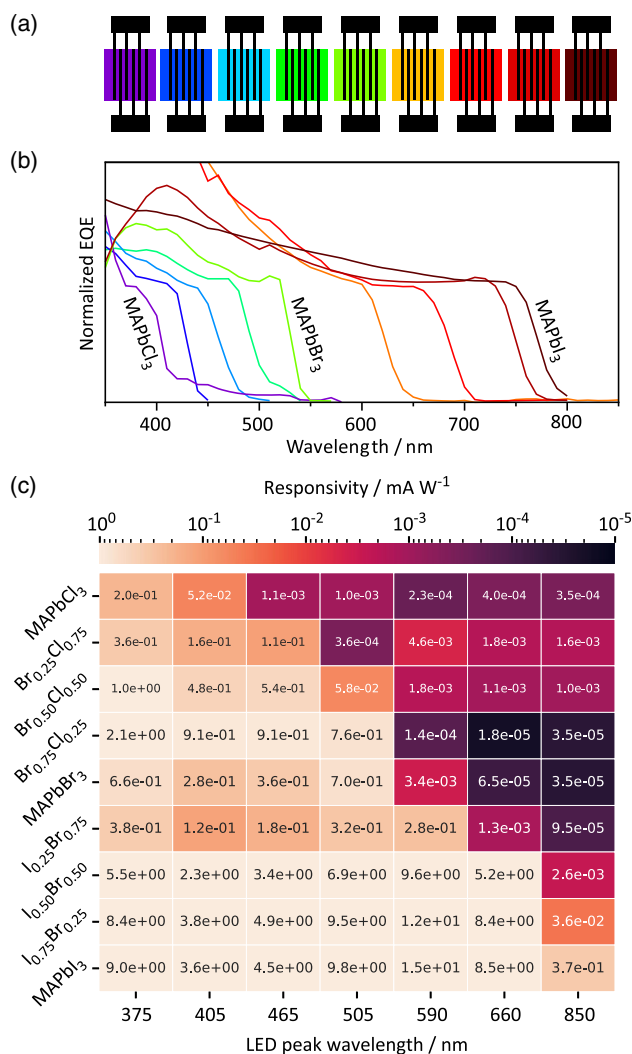


**Figure 3.** a) Each perovskite composition is inkjet printed onto prefabricated interdigitated ITO electrodes to produce a series of nine photodetectors. b) The detection onset of the photodetectors measured in EQE directly relates to the absorption onset of the printed layers and, in turn, the compositional gradient of the metal halide perovskite. c) The resulting selectivity of the photodetectors is confirmed by external excitation using high-powered LEDs. A jump in responsivity of multiple orders of magnitude (as shown by a change from dark to light colors in the grid) signals the absorption onset.

absorption onset toward higher wavelengths, an increasing number of LEDs induce a photocurrent (0.2–25  $\mu\text{A}$ ), which is higher than the dark current (0.1–10 nA).

By now dividing the difference of photocurrent and dark current (in A) at 5 V by the nominal power (in W) of the LED, a responsivity (in  $\text{A W}^{-1}$ ) can be calculated, as depicted in Figure 3c for each perovskite composition and LED excitation. The result is a matrix of responsivity values, with the perovskite composition on the y-axis and the excitation wavelength on the x-axis. The magnitude of the values is indicated by a color scale, dark colors correspond to a low responsivity ( $10^{-3}$ – $10^{-5}$   $\text{mA W}^{-1}$ ), while the lighter the color, the higher the responsivity (up to  $9.8 \text{ mA W}^{-1}$ ). As with the EQE, the responsivity is dependent

on the wavelength of the incident LED light. Once the photodetector is illuminated with the LED matching the absorption onset of the absorber material, a rise in responsivity by 2–3 orders of magnitude can be observed, comparable with previously reported values at comparable irradiance.<sup>[65–67]</sup>

Let us consider possible applications of this observation. When operated individually, the responsivity of a single photodetector provides limited information (high/low responsivity). However, when considering an entire column of responsivities within the matrix, the collective response of all nine photodetectors to one LED (with its particular wavelength) can be seen. Collectively, the photodetector series can there give a distinct response depending on the wavelength of the incident light. Depending on the resolution of the printed gradient and the calibration with different light sources, a combination of these photodetectors lays the foundation for use in the visible light spectrometer, without the need for a dispersion element.

### 3. Conclusion

In this work, we use combinatorial inkjet printing as a versatile tool to integrate a seamless gradient of metal halide perovskites in photodetector devices. Printing with multiple printheads and multiple inks and exploiting the DoD capabilities of inkjet printing result in precise control of the droplet ratio on the substrate. The deposited ink mixtures crystallize into distinct phase-pure perovskite thin films, producing a compositional halide gradient ranging from MAPbCl<sub>3</sub> via MAPbBr<sub>3</sub> to MAPbI<sub>3</sub>. The resulting perovskite compositions show a tunable bandgap between 410 and 790 nm, covering the full visible spectrum. Fine tuning of the ink ratio allows shifting of the bandgap by 8 nm increments within the chloride series at short wavelengths. Using these compositions, perovskite-based photodetectors were fabricated, which showed a spectral selectivity corresponding to the respective bandgap. When illuminated with an external light source with a wavelength lower than the absorption onset of the used perovskite composition, a photocurrent is measurable. A distinct photoresponse matrix is obtained when using a range of light sources to illuminate the series of photodetectors along the perovskite gradient. These findings pave the way for integration of the devices in a perovskite-based, dispersion element-free, visible light spectrometer.

### 4. Experimental Section

**Ink Preparation:** Weighing of precursor salts and solution preparation took place in a nitrogen-filled glovebox. Perovskite precursors were purchased from TCI (PbI<sub>2</sub>, PbBr<sub>2</sub>, PbCl<sub>2</sub>) and Dyanamo (MAI, MABr, MACl) and used as received. Anhydrous DMF and DMSO were purchased from Sigma Aldrich. MAPbI<sub>3</sub>, MAPbBr<sub>3</sub>, and MAPbCl<sub>3</sub> solution were prepared by dissolving PbI<sub>2</sub> and PbBr<sub>2</sub> in a solvent mixture of four parts DMF and one part DMSO and PbCl<sub>2</sub> in pure DMSO. Dissolving took place over several hours at 60 °C. The lead halide solutions were used to dissolve MAI, MABr, and MACl, resulting in pure halide perovskite precursor solutions. Precursor amounts were calculated to yield 1 M inks of equimolar mixed precursor salts.

**Sample Preparation:** Soda lime glass slides with an edge length of 25 mm were cleaned by sonication in aqueous Hellmanex II solution, acetone, and isopropanol and subsequently cleaned in a UV ozone cleaner (Ossila) for 30 min. The cleaned glass substrates were transferred to a nitrogen-filled glovebox with <0.1 ppm oxygen and <0.5 ppm water content. For device preparation, glass substrates with prepatterned ITO

electrodes (Ossila) were treated the same way. The interdigitated electrodes had a channel length of 50  $\mu\text{m}$  and channel width of 6  $\mu\text{m}$ .

**Printing Procedure:** A Pixdro LP 50 (Süss Microtec) with a dual head system of Spectra SE128 printheads (30  $\mu\text{L}$  droplet size) was used for thin-film preparation. To create a compositional gradient, the two printheads were filled with  $\text{MAPbI}_3$  and  $\text{MAPbBr}_3$  or  $\text{MAPbBr}_3$  and  $\text{MAPbCl}_3$ . The ink ratio was controlled by custom-created patterns that ensured even spread of both inks over the substrate. Both printheads received separate custom-created print patterns in which the pixel ratio mirrored the nominal ratio of halides in the solid film. Best results were obtained at a printing resolution of 250 dpi, print speed of 100  $\text{mm s}^{-1}$ , and droplet velocity of 4.0  $\text{m s}^{-1}$ . To ensure exact drop placement, a quality factor of 1 and unidirectional printing were chosen. After printing, the substrates were thermally treated to dry the films for 10 min on a hot plate at 100  $^\circ\text{C}$  for iodide-containing samples and 80  $^\circ\text{C}$  for chloride-containing samples. The substrates prepared with ITO electrodes and used as photodetector devices were encapsulated using a commercially available resin and hardened with a blue LED (Blufixx).

**Thin-Film Characterization:** UV/vis spectra were measured using a Lambda1050 system from PerkinElmer with an integrating sphere, with a spot size of 5 mm diameter. The absorption onset was determined via the first derivative of the spectrum. The resulting peak was fit with a pseudo-Voigt function and FWHM was extracted. Additional fitting of the absorption onset via the Elliot equation was carried out, to obtain the bandgap energy and exciton binding energy. Ionization energy and WF were measured by UPS in an Omicron system equipped with a hemispherical energy analyzer (SPECS Phoibos 100) using the He I emission (21.2 eV) as excitation source with an 80% intensity aluminum filter. The samples were ground during the measurements of the VB region, while a bias of  $-10\text{ V}$  was applied during the measurements of the WF calculated through the secondary electron cutoff. The ionization energy of the perovskite samples was also measured by PYS performed in air using the AC-2E DC 1 set-up from Riken Keiki. Measurements were performed in ambient atmosphere, using a UV lamp, with an excitation energy between 4 and 6 eV. XRD experiments were performed on a Bruker Advanced D8 in Bragg-Brentano geometry under ambient conditions with a  $\text{Cu K}\alpha$  X-ray source ( $\lambda = 1.5406\text{ \AA}$ ). The first main reflection peak was fit with a pseudo-Voigt function and FWHM was extracted. SEM images and EDX measurements were performed on an eLINE Plus electron beam lithography system from Raith. An acceleration voltage of 10 kV was used, with an aperture size of 30  $\mu\text{m}$  at a working distance of 10  $\mu\text{m}$  and a pressure of  $10^{-7}$  mbar. For the EDX maps, the intensities of the lead M $\alpha$  line, chlorine K $\alpha$  line, bromine L line, and iodine L $\alpha$  line were used to indicate the presence of the respective elements. The EDX maps had a size of 512 pixels, resulting in a resolution of 100  $\mu\text{m}$  per pixel.

**EQE Measurement:** The EQE was performed in ambient air using a SpeQuest Quantum Efficiency setup from Rera Systems. A 100 W tungsten halogen lamp was used as excitation source. The photodetector devices were biased with 30 V from an external source measure unit (Keithley 2602A source meter). The absolute EQE was calculated by reference measurement of a calibrated silicon solar cell (Rera Systems) at short-circuit conditions.

**Electrical Device Characterization:** The electrical characterization of the photodetector devices was done using a Keithley 4200A-SCS Parameter Analyzer and an Ossila push-fit test board. The devices were illuminated using a series of mounted ThorLabs LEDs, with the wavelength and irradiance given in brackets: M375L4 (375 nm, 137  $\text{mW cm}^{-2}$ ), M405L3 (405 nm, 336  $\text{mW cm}^{-2}$ ), M455L3 (455 nm, 312  $\text{mW cm}^{-2}$ ), M505L3 (505 nm, 111  $\text{mW cm}^{-2}$ ), M590L3 (590 nm, 53  $\text{mW cm}^{-2}$ ), M660L4 (660 nm, 174  $\text{mW cm}^{-2}$ ), and M850L3 (850 nm, 191  $\text{mW cm}^{-2}$ ). The LEDs were driven with 1 A while mounted at a distance of 2 cm from the device. The current–voltage characteristics were measured from  $-5$  to 5 V. The photocurrent at 5 V was used for the calculation of responsivity.

## Supporting Information

Supporting Information is available from the Wiley Online Library or from the author.

## Acknowledgements

This work was carried out in the framework of the Joint Lab GEN\_FAB and with the support of the Helmholtz Innovation Lab HySPRINT. The authors would like to thank Norbert Koch for granting instrument access. C. R., H. N., and E. L. U. acknowledge funding from the German Ministry of Education and Research (BMBF) for the Young Investigator Group Hybrid Materials Formation and Scaling (HyPerFORME) within the program “NanoMatFutur” (03XP0091), as well as the Helmholtz Energy Materials Foundry (HEMF) and PEROSEED (ZT-0024) project.

Open access funding enabled and organized by Projekt DEAL.

## Conflict of Interest

The authors declare no conflict of interest.

## Data Availability Statement

All data is provided in the supporting information file.

## Keywords

bandgap tunability, combinatorial inkjet printing, halide variations, metal halide perovskites, wavelength-selective photodetectors

Received: October 14, 2021

Published online: December 2, 2021

- [1] J. Y. Kim, J. W. Lee, H. S. Jung, H. Shin, N. G. Park, *Chem. Rev.* **2020**, 120, 7867.
- [2] M. Saliba, T. Matsui, J. Y. Seo, K. Domanski, J. P. Correa-Baena, M. K. Nazeeruddin, S. M. Zakeeruddin, W. Tress, A. Abate, A. Hagfeldt, M. Grätzel, *Energy Environ. Sci.* **2016**, 9, 1989.
- [3] S. Shao, M. A. Loi, *Adv. Mater. Interfaces* **2020**, 7, 1901469.
- [4] R. H. Friend, D. Di, S. Lilliu, B. Zhao, *Sci. Video Protoc.* **2019**, 1, 1.
- [5] A. Sadhanala, S. Ahmad, B. Zhao, N. Giesbrecht, P. M. Pearce, F. Deschler, R. L. Z. Hoyer, K. C. Gödel, T. Bein, P. Docampo, S. E. Dutton, M. F. L. De Volder, R. H. Friend, *Nano Lett.* **2015**, 15, 6095.
- [6] S. G. R. Bade, J. Li, X. Shan, Y. Ling, Y. Tian, T. Dilbeck, T. Besara, T. Geske, H. Gao, B. Ma, K. Hanson, T. Siegrist, C. Xu, Z. Yu, *ACS Nano* **2016**, 10, 1795.
- [7] L. Lei, Q. Dong, K. Gundogdu, F. So, *Adv. Funct. Mater.* **2021**, 31, 1.
- [8] C. Cho, T. Antrick, M. Kroll, Q. An, T. R. Bärschneider, A. Fischer, S. Meister, Y. Vaynzof, K. Leo, *Adv. Sci.* **2021**, 2101663, 1.
- [9] M. Saliba, S. M. Wood, J. B. Patel, P. K. Nayak, J. Huang, J. A. Alexander-Webber, B. Wenger, S. D. Stranks, M. T. Hörantner, J. T. W. Wang, R. J. Nicholas, L. M. Herz, M. B. Johnston, S. M. Morris, H. J. Snaith, M. K. Riede, *Adv. Mater.* **2016**, 28, 923.
- [10] H. Wei, J. Huang, *Nat. Commun.* **2019**, 10, 1.
- [11] S. Yakunin, M. Sytnyk, D. Kriegner, S. Shrestha, M. Richter, G. J. Matt, H. Azimi, C. J. Brabec, J. Stangl, M. V. Kovalenko, W. Heiss, *Nat. Photonics* **2015**, 9, 444.
- [12] Y. C. Kim, K. H. Kim, D. Y. Son, D. N. Jeong, J. Y. Seo, Y. S. Choi, I. T. Han, S. Y. Lee, N. G. Park, *Nature* **2017**, 550, 87.
- [13] J. Miao, F. Zhang, *J. Mater. Chem. C* **2019**, 7, 1741.
- [14] S. Tong, C. Gong, C. Zhang, G. Liu, D. Zhang, C. Zhou, J. Sun, S. Xiao, J. He, Y. Gao, J. Yang, *Appl. Mater. Today* **2019**, 15, 389.

- [15] F. Tang, Q. Chen, L. Chen, F. Ye, J. Cai, L. Chen, *Appl. Phys. Lett.* **2016**, *109*, 123301.
- [16] L. M. Herz, *ACS Energy Lett.* **2017**, *2*, 1539.
- [17] M. Zhang, H. Yu, M. Lyu, Q. Wang, J. H. Yun, L. Wang, *Chem. Commun.* **2014**, *50*, 11727.
- [18] R. Prasanna, A. Gold-Parker, T. Leijtens, B. Conings, A. Babayigit, H. G. Boyen, M. F. Toney, M. D. McGehee, *J. Am. Chem. Soc.* **2017**, *139*, 11117.
- [19] S. A. Kulkarni, T. Baikie, P. P. Boix, N. Yantara, N. Mathews, S. Mhaisalkar, *J. Mater. Chem. A* **2014**, *2*, 9221.
- [20] A. Al-Ashouri, E. Köhnen, B. Li, A. Magomedov, H. Hempel, P. Caprioglio, J. A. Márquez, A. B. M. Vilches, E. Kasparavicius, J. A. Smith, N. Phung, D. Menzel, M. Grischek, L. Kegelmann, D. Skroblin, C. Gollwitzer, T. Malinauskas, M. Jošt, G. Matič, B. Rech, R. Schlattmann, M. Topič, L. Korte, A. Abate, B. Stannowski, D. Neher, M. Stolterfoht, T. Unold, V. Getautis, S. Albrecht, *Science* **2020**, *370*, 1300.
- [21] M. Jošt, T. Bertram, D. Koushik, J. A. Marquez, M. A. Verheijen, M. D. Heinemann, E. Köhnen, A. Al-Ashouri, S. Braunger, F. Lang, B. Rech, T. Unold, M. Creatore, I. Laueremann, C. A. Kaufmann, R. Schlattmann, S. Albrecht, *ACS Energy Lett.* **2019**, *4*, 583.
- [22] K. Lin, J. Xing, L. N. Quan, F. P. G. de Arquer, X. Gong, J. Lu, L. Xie, W. Zhao, D. Zhang, C. Yan, W. Li, X. Liu, Y. Lu, J. Kirman, E. H. Sargent, Q. Xiong, Z. Wei, *Nature* **2018**, *562*, 245.
- [23] B. Han, S. Yuan, B. Cai, J. Song, W. Liu, F. Zhang, T. Fang, C. Wei, H. Zeng, *Adv. Funct. Mater.* **2021**, *2011003*, 1.
- [24] L. Cheng, C. Yi, Y. Tong, L. Zhu, G. Kusch, X. Wang, X. Wang, T. Jiang, H. Zhang, J. Zhang, C. Xue, H. Chen, W. Xu, D. Liu, R. A. Oliver, R. H. Friend, L. Zhang, N. Wang, W. Huang, J. Wang, *Research* **2020**, *2020*, 1.
- [25] X. Zhao, Z. K. Tan, *Nat. Photonics* **2020**, *14*, 215.
- [26] H. Näsström, P. Becker, J. A. Márquez, O. Shargaieva, R. Mainz, E. Unger, T. Unold, *J. Mater. Chem. A* **2020**, *8*, 22626.
- [27] A. Teichler, J. Perelaer, U. S. Schubert, *Macromol. Chem. Phys.* **2013**, *214*, 547.
- [28] A. Queraltó, J. Banchewski, A. Pacheco, K. Gupta, L. Saltarelli, D. Garcia, N. Alcalde, C. Mocuta, S. Ricart, F. Pino, X. Obradors, T. Puig, *ACS Appl. Mater. Interfaces* **2021**, *13*, 9101.
- [29] F. Hermerschmidt, P. Papagiorgis, A. Savva, C. Christodoulou, G. Itskos, S. A. Choulis, *Sol. Energy Mater. Sol. Cells* **2014**, *130*, 474.
- [30] M. Böberl, M. V. Kovalenko, S. Gamerith, E. J. W. List, W. Heiss, *Adv. Mater.* **2007**, *19*, 3574.
- [31] F. Hermerschmidt, D. Burmeister, G. Ligorio, S. M. Pozov, R. Ward, S. A. Choulis, E. J. W. List-Kratochvil, *Adv. Mater. Technol.* **2018**, *3*, 1.
- [32] S. Gamerith, A. Klug, H. Scheiber, U. Scherf, E. Moderegger, E. J. W. List, *Adv. Funct. Mater.* **2007**, *17*, 3111.
- [33] W. Yang, E. J. W. List-Kratochvil, C. Wang, *J. Mater. Chem. C* **2019**, *7*, 15098.
- [34] S. Jung, A. Sou, K. Banger, D. H. Ko, P. C. Y. Chow, C. R. McNeill, H. Siringhaus, *Adv. Energy Mater.* **2014**, *4*, 1400432.
- [35] E. Fisslthaler, S. Sax, U. Scherf, G. Mauthner, E. Moderegger, K. Landfester, E. J. W. List, *Appl. Phys. Lett.* **2008**, *92*, 1.
- [36] L. Kinner, S. Nau, K. Popovic, S. Sax, I. Burgués-Ceballos, F. Hermerschmidt, A. Lange, C. Boeffel, S. A. Choulis, E. J. W. List-Kratochvil, *Appl. Phys. Lett.* **2017**, *110*, 101107.
- [37] M. Hengge, K. Livanov, N. Zamoshchik, F. Hermerschmidt, E. J. W. List-Kratochvil, *Flexible Printed Electron.* **2021**, *6*, 015009.
- [38] F. Mathies, E. J. W. List-Kratochvil, E. L. Unger, *Energy Technol.* **2020**, *8*, 1900991.
- [39] F. Hermerschmidt, F. Mathies, V. R. F. Schröder, C. Rehermann, N. Z. Morales, E. L. Unger, E. J. W. List-Kratochvil, *Mater. Horizons* **2020**, *7*, 1773.
- [40] M. Min, R. F. Hossain, N. Adhikari, A. B. Kaul, *ACS Appl. Mater. Interfaces* **2020**, *12*, 10809.
- [41] Y. Liu, F. Li, C. Perumal Veeramalai, W. Chen, T. Guo, C. Wu, T. W. Kim, *ACS Appl. Mater. Interfaces* **2017**, *9*, 11662.
- [42] T. M. Eggenhuisen, Y. Galagan, A. F. K. V. Biezemans, T. M. W. L. Slaats, W. P. Voorthuizen, S. Kommeren, S. Shanmugam, J. P. Teunissen, A. Hadipour, W. J. H. Verhees, S. C. Veenstra, M. J. J. Coenen, J. Gilot, R. Andriessen, W. A. Groen, *J. Mater. Chem. A* **2015**, *3*, 7255.
- [43] R. Eckstein, N. Strobel, T. Rödlmeier, K. Glaser, U. Lemmer, G. Hernandez-Sosa, *Adv. Opt. Mater.* **2018**, *6*, 1.
- [44] A. C. Arias, J. D. MacKenzie, I. McCulloch, J. Rivnay, A. Salleo, *Chem. Rev.* **2010**, *110*, 3.
- [45] S. Chen, L. Zhang, L. Yan, X. Xiang, X. Zhao, S. Yang, B. Xu, *Adv. Funct. Mater.* **2019**, *29*, 1905487.
- [46] M. Bag, Z. Jiang, L. A. Renna, S. P. Jeong, V. M. Rotello, D. Venkataraman, *Mater. Lett.* **2016**, *164*, 472.
- [47] H. Näsström, O. Shargaieva, P. Becker, F. Mathies, I. Zizak, V. R. F. Schröder, E. J. W. List-Kratochvil, T. Unold, E. L. Unger, Submitted.
- [48] R. D. Deegan, O. Bakajin, T. F. Dupont, G. Huber, S. R. Nagel, T. A. Witten, *Nature* **1997**, *389*, 827.
- [49] F. Mathies, E. R. Nandayapa, G. Paramasivam, M. F. Al Rayes, V. R. F. Schröder, C. Rehermann, E. J. W. List-Kratochvil, E. L. Unger, *Mater. Adv.* **2021**, *2*, 5365.
- [50] N. Ahn, D. Y. Son, I. H. Jang, S. M. Kang, M. Choi, N. G. Park, *J. Am. Chem. Soc.* **2015**, *137*, 8696.
- [51] H. W. King, Y. Lo Vegard, *J. Mater. Sci.* **1921**, *1*, 79.
- [52] A. Poglitsch, D. Weber, *J. Chem. Phys.* **1987**, *87*, 6373.
- [53] B. W. Park, S. M. Jain, X. Zhang, A. Hagfeldt, G. Boschloo, T. Edvinsson, *ACS Nano* **2015**, *9*, 2088.
- [54] C. Li, J. Wei, M. Sato, H. Koike, Z. Z. Xie, Y. Q. Li, K. Kanai, S. Kera, N. Ueno, J. X. Tang, *ACS Appl. Mater. Interfaces* **2016**, *8*, 11526.
- [55] C. Rehermann, A. Merdasa, K. Suchan, V. Schröder, F. Mathies, E. L. Unger, *ACS Appl. Mater. Interfaces* **2020**, *12*, 30343.
- [56] F. Lehmann, A. Franz, D. M. Többens, S. Levcenko, T. Unold, A. Taubert, S. Schorr, *RSC Adv.* **2019**, *9*, 11151.
- [57] M. Saba, F. Quochi, A. Mura, G. Bongiovanni, *Acc. Chem. Res.* **2016**, *49*, 166.
- [58] A. M. Soufiani, F. Huang, P. Reece, R. Sheng, A. Ho-Baillie, M. A. Green, *Appl. Phys. Lett.* **2015**, *107*, 231902.
- [59] I. Anusca, S. Balčiūnas, P. Gemeiner, Š. Svirskas, M. Sanlialp, G. Lackner, C. Fettkenhauer, J. Belovickis, V. Samulionis, M. Ivanov, B. Dkhil, J. Banyas, V. V. Shvartsman, D. C. Lupascu, *Adv. Energy Mater.* **2017**, *7*, 1.
- [60] M. Sendner, P. K. Nayak, D. A. Egger, S. Beck, C. Müller, B. Epling, W. Kowalsky, L. Kronik, H. J. Snaith, A. Pucci, R. Lovrinčić, *Mater. Horiz.* **2016**, *3*, 613.
- [61] J. D. Jackson, *Classical Electrodynamics*, John Wiley & Sons, Inc., New York **1962**.
- [62] O. Almora, C. I. Cabrera, J. Garcia-Cerrillo, T. Kirchartz, U. Rau, C. J. Brabec, *Adv. Energy Mater.* **2021**, *11*, 2100022.
- [63] S. Tao, I. Schmidt, G. Brocks, J. Jiang, I. Tranca, K. Meerholz, S. Olthof, *Nat. Commun.* **2019**, *10*, 1.
- [64] J. Endres, D. A. Egger, M. Kulbak, R. A. Kerner, L. Zhao, S. H. Silver, G. Hodes, B. P. Rand, D. Cahen, L. Kronik, A. Kahn, *J. Phys. Chem. Lett.* **2016**, *7*, 2722.
- [65] F. Wang, J. Mei, Y. Wang, L. Zhang, H. Zhao, D. Zhao, *ACS Appl. Mater. Interfaces* **2016**, *8*, 2840.
- [66] Y. Chen, C. Zhao, T. Zhang, X. Wu, W. Zhang, S. J. Ding, *Small* **2021**, *2007543*, 1.
- [67] E. Horváth, M. Spina, Z. Szekrényes, K. Kamarás, R. Gaal, D. Gachet, L. Forró, *Nano Lett.* **2014**, *14*, 6761.